nature nanotechnology

Article

https://doi.org/10.1038/s41565-023-01436-w

Molecular machines stimulate intercellular calcium waves and cause muscle contraction

Received: 7 November 2022

Accepted: 3 May 2023

Published online: 10 July 2023

Check for updates

Jacob L. Beckham[1], Alexis R. van Venrooy[1], Soonyoung Kim[2], Gang Li[1], Bowen Li[1], Guillaume Duret[2], Dallin Arnold[1], Xuan Zhao[2], John T. Li[1], Ana L. Santos[1,3], Gautam Chaudhry[1], Dongdong Liu[1], Jacob T. Robinson[4] ✉ & James M. Tour[5] ✉

Intercellular calcium waves (ICW) are complex signalling phenomena that control many essential biological activities, including smooth muscle contraction, vesicle secretion, gene expression and changes in neuronal excitability. Accordingly, the remote stimulation of ICW could result in versatile biomodulation and therapeutic strategies. Here we demonstrate that light-activated molecular machines (MM)—molecules that perform mechanical work on the molecular scale—can remotely stimulate ICW. MM consist of a polycyclic rotor and stator that rotate around a central alkene when activated with visible light. Live-cell calcium-tracking and pharmacological experiments reveal that MM-induced ICW are driven by the activation of inositol-triphosphate-mediated signalling pathways by unidirectional, fast-rotating MM. Our data suggest that MM-induced ICW can control muscle contraction in vitro in cardiomyocytes and animal behaviour in vivo in *Hydra vulgaris*. This work demonstrates a strategy for directly controlling cell signalling and downstream biological function using molecular-scale devices.

Calcium signalling impacts nearly every process relevant to cellular life, and the ability of calcium ions to alter protein shape and charge by reversible binding constitutes the most ubiquitous signalling motif in receptor biology[1]. The localized nature of calcium signalling, as well as its ability to activate downstream effector proteins, allows it to drive a vast array of biological processes. In single cells, calcium directly controls cellular proliferation[2], gene expression[3,4], differentiation[5], movement[6] and metabolism[7]. In organisms, calcium signals propagate through secondary messengers to cause intercellular calcium waves (ICW) that coordinate concerted action in whole tissues[8]. ICW play direct or indirect roles in processes ranging from muscle contraction[9], potentiation of neuronal firing[10], blood vessel dilation[11], digestion[12] and breathing[13]. Dysfunctional calcium signalling contributes to disease states ranging from cancer to cardiovascular disease and neurodegenerative disorders[14,15].

Due to the multiplexed nature of calcium signalling[16], the ability to remotely trigger ICW with high spatiotemporal precision may permit access to numerous downstream signalling pathways, offering a dynamic new strategy for the control of biological activity. Such advances may also yield new therapeutic avenues for diseases characterized by calcium signalling dysfunction. Currently, ICW are largely initiated experimentally by chemical methods[17] or by applying mechanical stimuli using a micropipette attached to a microcontroller[2,8,18].

Here we describe the generation of ICW via the nanomechanical action of light-activated molecular machines (MM). MM are molecules that can be activated by external stimuli, such as light, to perform

[1]Department of Chemistry, Rice University, Houston, TX, USA. [2]Department of Electrical Engineering, Rice University, Houston, TX, USA. [3]IdISBA—Fundación de Investigación Sanitaria de las Islas Baleares, Palma, Spain. [4]Department of Bioengineering, Department of Electrical Engineering, Rice University, Houston, TX, USA. [5]Department of Chemistry, Smalley-Curl Institute, NanoCarbon Center and Rice Advanced Materials Institute, Department of Materials Science and Nanoengineering, Department of Computer Science, Rice University, Houston, TX, USA. ✉e-mail: jacob.t.robinson@rice.edu; tour@rice.edu

https://doi.org/10.1038/s41565-023-01436-w

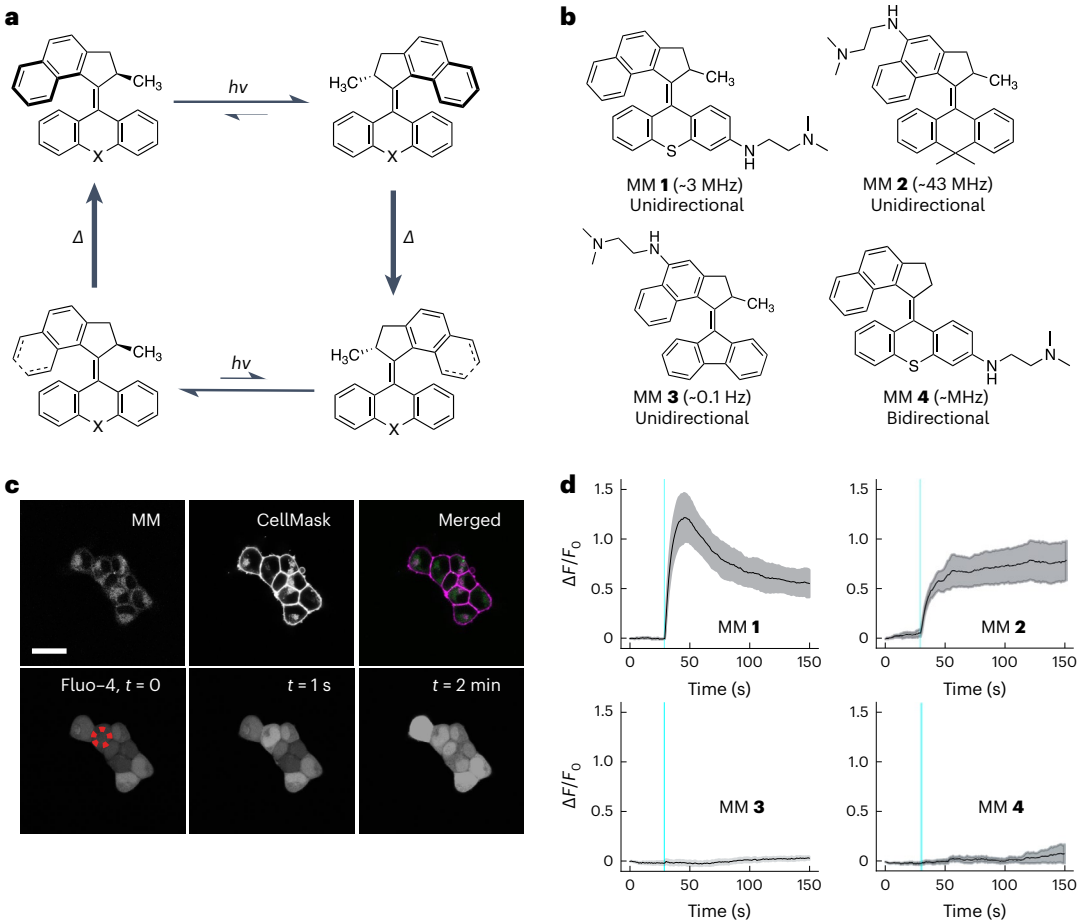

Fig. 1 | Structures of MM used in this study, their mechanism of rotation and their activation to induce calcium waves in HEK293 cells. a, Rotation cycle of a typical MM, showing two photoisomerizations (*hv*) and two thermal (*Δ*) helix inversions to complete a unidirectional rotation. The moiety in the 'X' position can be changed to synthesize MM of different rotation speeds. **b**, Structures of the MM employed in this study. MM **1** and MM **2** complete fast (megahertz-scale) unidirectional rotation. MM **3** rotates at 0.1 Hz at room temperature. MM **4** lacks chirality imparted by the allylic methyl and possesses no preference for unidirectional rotation. **c**, Confocal microscopy images of cells treated with MM **1**, calcium-tracking dye Fluo-4 and cell-membrane-labelling dye CellMask (used to differentiate individual cells), showing a rapid increase in intracellular calcium levels after stimulation with 400 nm light. The red dotted circle labels the area of laser stimulation. The images in the top row were taken before stimulation, and the images in the bottom row were taken immediately before, 1 s after and 2 min after stimulation. Scale bar (all images), 20 µm. **d**, Representative normalized fluorescence intensity traces of Fluo-4 in HEK293 cells treated with each MM. The solid line represents the average responses of $n = 6$ independent cells, and the shaded area represents the standard error of the mean. MM **1**, MM **2** and MM **4** were administered to cells at 8 µM. MM **3** was administered to cells at 24 µM. Stimuli for cells treated with MM **1**, **2** and **4** used a 250 ms pulse width delivered to a circular area of diameter 5 µm at 3.2×10^2 W cm^{-2}. Stimuli for cells treated with MM **3** were administered at 6.4×10^2 W cm^{-2}. For all the plots, the cyan line indicates the time of stimulus presentation.

mechanical work on the molecular scale[19]. Just as the mechanical perturbation of a cell's outer membrane causes intracellular calcium responses, the application of a mechanical force via a fast, unidirectionally rotating MM elicits calcium release from the endoplasmic reticulum (ER). These MM-induced ICW can be exploited to control downstream biological processes, like muscle contraction, both in vitro and in vivo.

Results and discussion

Fast, unidirectional MM induce calcium waves in vitro

MM employed in this study have overcrowded alkene motors based on the primary design described in another work[19]. Their typical structure consists of a rotor connected to a stator by an atropisomeric alkene. When these MM are excited by incident photons, the rotor rotates unidirectionally relative to the stator, undergoing two photoisomerization steps and two thermal helix inversions before returning to the starting position (Fig. 1a). Overcrowded alkene motors locomote in solution[20], drill through synthetic lipid bilayers and cell membranes[21] and have previously been used to exert mechanical forces on cell-surface receptors via antibody targeting[22]. Here we study cellular responses to MM administered without the use of chemical targeting or extracellular scaffolds, facilitating their use in vivo. The moiety 'X' (Fig. 1a) can be interchanged to modulate the MM rotation rate, which is determined by the favourability of the thermal helix inversion step[23,24]. The structures of the MM used in this study are shown in Fig. 1b. These MM possess an appended aniline that shifts their absorption into the visible spectrum, enabling their observation by visible-light microscopy and the activation of their rotation with visible light[25].

To investigate cellular responses to the actuation of MM, we employed live-cell calcium tracking. HEK293 cells were treated with the fluorescent intracellular calcium indicator Fluo-4 and incubated with MM. MM were internalized within the cells by a combination of passive and active transport mechanisms (Supplementary Fig. 1). The calcium responses of cells treated with fast-rotating MM **1** are shown in Fig. 1c. Stimulation of a single MM **1**-treated cell with a 400 nm laser (3.2×10^2 W cm^{-2}) increased the Fluo-4 fluorescence in the targeted cell, reflecting a spike in the intracellular calcium concentration similar to that observed when cells are mechanically perturbed

with a micropipette[8,18]. In the presence of the solvent only, no calcium responses were evoked by the same laser treatment (Supplementary Fig. 2). Calcium responses propagated to adjacent cells (Supplementary Fig. 3) according to the degree of electrical connectivity between individual colonies. Similar responses were observed when cells were treated with reactive oxygen species scavengers (Supplementary Fig. 4) and in experiments using X-Rhod-1 in place of Fluo-4 (Supplementary Fig. 5), suggesting that the observed responses do not depend on the production of singlet oxygen or fluorescence resonant energy transfer between MM **1** and calcium-tracking dyes.

Cellular responses to MM were repeatable (Supplementary Fig. 6), and their amplitude could be controlled by the intensity of incident light (Supplementary Fig. 7). The strength of the evoked response also determines the downstream effects of stimulation. At typical stimulation irradiances (3.2×10^2 W cm^{-2} for 250 ms), cells recovered from stimulation and showed no signs of apoptosis or necrosis (Supplementary Figs. 8 and 9 and the accompanying discussion). The cells stimulated at higher intensities (6.4×10^2 W cm^{-2} for 4 s) showed membrane blebbing and calcium accumulation over a 30 min period, indicating cell death (Supplementary Fig. 10)[26]. Hence, MM-induced ICW can be tuned between physiological, supraphysiological and pathophysiological response regimes by adjusting the stimulus intensity. Calcium responses induced by MM **1** actuation were also observed in other cell lines (Supplementary Figs. 11 and 12).

We investigated the calcium responses elicited by a library of MM consisting of two fast-rotating motors (MM **1**–**2**) and two complementary motors (MM **3**–**4**) used to test the effects of rotation speed and directionality (Fig. 1b). These MM were designed to mimic molecules with previously reported rotary properties. We supplemented our investigation with a qualitative study of the rotary properties of each molecule using density functional theory (Supplementary Fig. 13, Supplementary Videos 1–5, Supplementary Table 1 and the related discussion in Supplementary Information).

MM **1**, mimicking designs previously shown to kill cancer cells and antibiotic-resistant bacteria[25,27,28], was synthesized with a thioxanthene stator. MM **1** rotates unidirectionally at ~3 MHz (ref. 19). MM **2** and MM **3** are chemically like MM **1** but rotate at different rates. MM **2**, which rotates at ~43 MHz, was synthesized with an anthracene stator with two methyl groups branching off the central carbon atom[24]. MM **3**, a slow-rotating motor that rotates at ~0.1 Hz (ref. 24), was synthesized with a fluorene stator. Finally, MM **4** is an analogue of MM **1** that lacks a stereogenic centre at the allylic methyl site, which confers preference for unidirectional rotation. Without this stereogenic centre, MM **4** stochastically switches between symmetrical and energetically identical stable isomers. MM **4** also possesses an additional transition state that interrupts the thermal helix inversion of the molecule entirely (Supplementary Fig. 13 and Supplementary Video 5)[19]. Although the energy barriers to these transition states are low, the symmetry of the two photoisomers of MM **4** prevents unidirectional rotation.

Figure 1d shows the calcium responses of cells treated with each MM and light. MM **3** was used at 3× concentration because of its lower extinction coefficient relative to the other MM (Supplementary Fig. 14 and Supplementary Table 2). Fast-rotating MM **1** and MM **2** elicited rapid increases in intracellular calcium. MM **1** elicited high-amplitude transients that peak ~10–20 s after stimulation and then decay over the next minute, whereas MM **2** elicited a more stable increase in intracellular calcium that does not decay as quickly as MM **1**. The different calcium release kinetics induced by MM **1** and MM **2** may be related to differences in their photoisomerization efficiency (Supplementary Fig. 15 and the related discussion in Supplementary Information)[23]. Meanwhile, slow-rotating MM **3** elicited no change in calcium activity on irradiation, even at 3× the concentration and twice the stimulus intensity used to activate MM **1** and MM **2** (Fig. 1d). MM **4**, the fast-rotating motor with no preference for unidirectional rotation, elicited only small changes in calcium concentration. This experiment provides evidence to link MM rotation speed and directionality to their evoked cell signalling behaviour.

Mechanistic study of MM-induced ICW

Next, we studied the biological mechanism behind MM-driven calcium signalling. Calcium equilibrium in the cytosol is regulated by both export across the plasma membrane and uptake into the ER via membrane ATPases (Fig. 2a)[1]. Consequentially, the cytosolic concentration of calcium is typically low (~100 nM) compared with those found inside the ER or extracellular medium (~1.5 mM). Cytosolic calcium spikes commonly involve the entry of calcium from one of these two locations. Fluorescence microscopy showed that MM internalize within cells and interact with subcellular organelles, including mitochondria and the ER (Fig. 2b and Supplementary Figs. 16 and 17). Therefore, we hypothesized that MM-induced calcium responses arise from the release of calcium from intracellular stores. To test this hypothesis, we depleted calcium stores inside and outside of HEK293 cells and blocked various plasma membranes or ER calcium channels before stimulation (Supplementary Table 3 provides a complete list of the manipulations employed in these experiments).

Cells treated with MM **1** and stimulated by light in the absence of extracellular calcium (Fig. 2c) showed no differences in response amplitude compared with a positive control in a calcium-containing medium. Similar results were observed when the plasma membrane calcium channels were blocked in the calcium-containing medium. Treatment of cells with ruthenium red (RR), a pharmacological inhibitor of temperature-sensitive vanilloid transient receptor potential channels[29], did not decrease the magnitude of MM-induced calcium responses (Fig. 2d). Similarly, the treatment of cells with gadolinium (Gd^{3+}), which is commonly used to block the effects of mechanosensitive plasma membrane channels such as Piezo1, Piezo2 and TRPC4 (ref. 30), also did not affect the observed responses (Fig. 2e).

On the other hand, cells treated with MM **1** and thapsigargin (Th), a sarco-ER calcium pump antagonist that depletes intracellular calcium[31], did not show any measurable calcium flux on light stimulation (Fig. 2f; $P = 0.00257 < 0.01$). This result implies that MM-evoked calcium responses arise from the release of ER-bound calcium stores by MM **1**.

Further mechanistic studies were conducted to determine how MM activation releases calcium from the ER. The mammalian ER predominantly expresses two tetrameric calcium channels: the inositol-triphosphate (IP_3) receptor (IP_3R) and the ryanodine (Ry) receptor[1,32]. The treatment of cells with Ry (100 μM) to block Ry receptor signalling had no effect on the response amplitude (Fig. 2g) in HEK293 cells. However, the treatment of cells with xestospongin C (XeC; 25 μM), a known antagonist of IP_3R (ref. 33), diminished cellular responses to MM (Fig. 2h; $P = 0.0167 < 0.05$). Similar effects were observed when cells were treated with the phospholipase C (PLC) antagonist U-73122 (U-73; 10 μM) as an alternate method of blocking IP_3 signalling (Fig. 2i; $P = 0.0281 < 0.05$). MM-induced responses were also inhibited in cells treated with cytochalasin D (Cyto D; 2 μM), an inhibitor of F-actin polymerization that disrupts PLC signalling by increasing the spatial distance between PLC and IP_3R (Fig. 2j; $P = 0.01762 < 0.05$)[34].

These results implicate IP_3 signalling as the primary driver of MM-induced calcium waves. The IP_3 pathway is typically initiated by G-protein coupled receptors or tyrosine kinase receptors, which activate PLCβ to cleave phosphatidylinositol 4,5-biphosphate into diacylglycerol and IP_3 (ref. 32). IP_3 then binds to IP_3R and causes calcium release. Inhibiting G-protein-coupled receptor signalling with gallein (Gal; 100 μM) also diminished the cellular responses to MM (Fig. 2k; $P = 0.004392 < 0.01$), strengthening the hypothesis that MM-induced calcium transients are driven by IP_3 signalling.

The IP_3 pathway contributes to mechanosensitive calcium currents[35] and drives ICW in response to mechanical stimulation with a micropipette[2,18]. In these experiments, mechanical force causes a conformational change in a membrane-bound protein[2], which then

https://doi.org/10.1038/s41565-023-01436-w

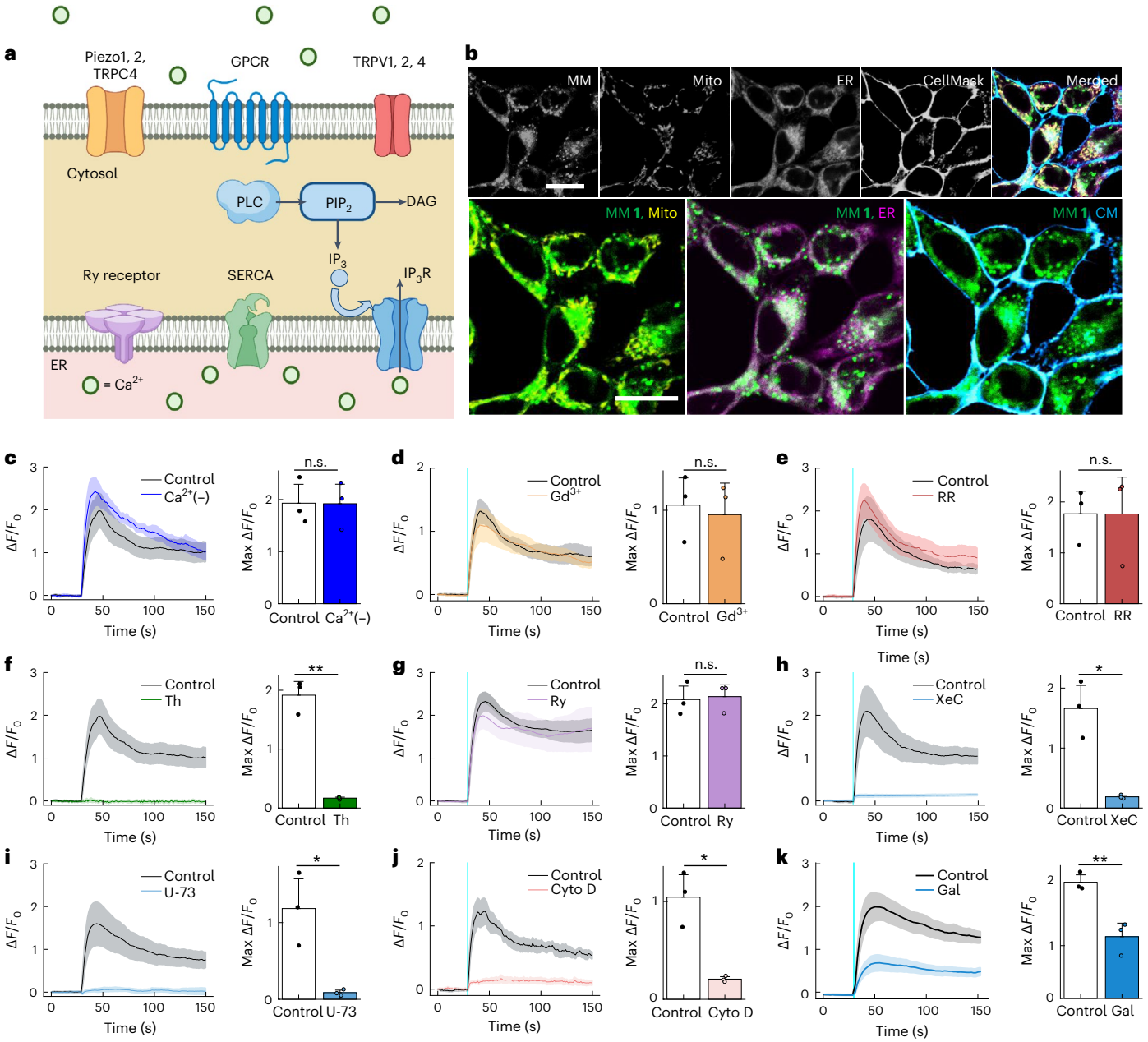

Fig. 2 | Mechanistic study of calcium waves induced by MM. a, Schematic of the possible mechanisms by which calcium can enter the cytoplasm. Prepared with Biorender.com. **b**, Confocal microscopy images of HEK293 cells treated with MM **1**, MitoTracker Green, ER-Tracker Red and CellMask Deep Red. Green, MM; yellow, mitochondria; magenta, ER; blue, cell membrane. Scale bar, 20 μm. **c**–**h**, Calcium waves elicited by MM **1**-treated cells in calcium-free PBS (**c**), in Gd^{3+} (50 μM) (**d**), in RR (10 μM) (**e**), after treatment of cells with Th (1 μM; $P = 0.00257 < 0.01$) (**f**), in Ry (100 μM) (**g**), in XeC (25 μM; $P = 0.0167 < 0.05$) (**h**), in U-73 (10 μM; $P = 0.0281 < 0.05$) (**i**), after pre-treatment of cells with Cyto D (2 μM; $P = 0.01762 < 0.05$) (**j**) and in Gal (100 μM; $P = 0.004392 < 0.01$) (**k**). The solid line represents the calcium profiles averaged from six independent cells. The shaded region represents the standard error of the mean ($n = 6$). Stimuli were presented after 30 s of imaging in each case, and the time of stimulus presentation is indicated by the vertical cyan line. For all the plots, the black trace shows a positive control consisting of MM **1**-treated cells in a typical imaging buffer recorded on the same day. All the stimuli were delivered with a pulse width of 250 ms to a circular area of diameter 5 μm at power ranging from 3.2×10^2 to 5.1×10^2 W cm^{-2}. For all the plots, the cyan line indicates the time of stimulus presentation. The controls and experimental groups were imaged and stimulated on the same day using the same conditions and with the same batch of cells. The error bars in the bar graphs represent the standard deviation of the mean of $n = 3$ experiments (at least six stimulated cells per experiment). Statistical analyses were performed using a one-tailed Welch's *t*-test. **P* value < 0.05, ***P* value < 0.01, ****P* value < 0.001, *****P* value < 0.0001. See Supplementary Table 3 for additional information on each pharmacological manipulation performed in these experiments.

activates PLCβ. Since MM locomote in solution at a rate of ~9 nm per revolution[20] and can exert forces of 10^{-12} to 10^{-9} N on their environment[21,22], they could feasibly initiate the same signalling cascade by exerting forces on the plasma membrane, the cytoskeleton or protein-bearing endosomes. Future experiments will further explore the biophysical interactions that drive cellular responses to MM.

MM cause muscle contraction in cardiomyocytes

Next, we investigated whether MM-elicited ICW could be used to modulate calcium-driven biological processes, such as muscle contraction. Figure 3 shows the effects of MM stimulation on primary rat cardiomyocytes. MM distribute to the sarcoplasmic reticulum (SR; Fig. 3a), where subsequent light activation triggers localized calcium release

https://doi.org/10.1038/s41565-023-01436-w

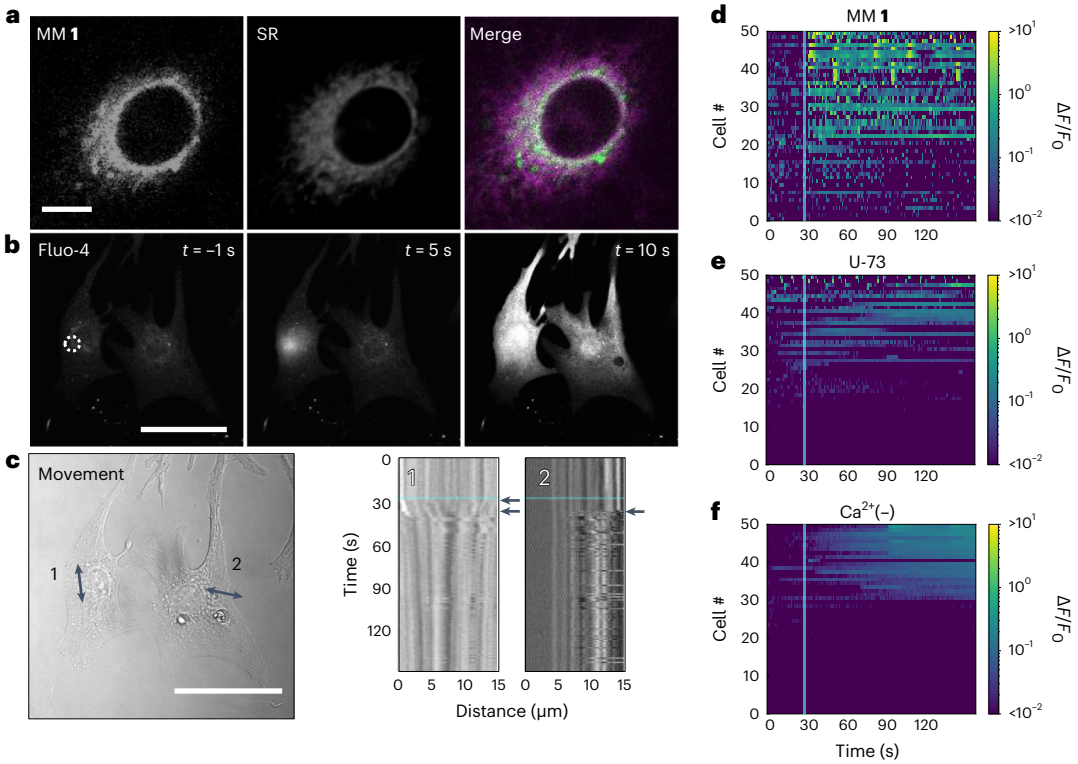

Fig. 3 | MM cause localized calcium release, contraction and beating in cardiomyocytes. a, Confocal microscopy images of a single myocyte treated with MM **1** and ER-Tracker Red. Green, MM; magenta, SR. Scale bar (all images), 10 μm. **b**, Confocal microscopy images showing Fluo-4 fluorescence, revealing calcium activity in cardiomyocytes before and after stimulation. Scale bar (all images), 50 μm. The white circle represents the stimulation region. **c**, Kymographs representative of cardiac myocyte contractile responses from the same cells shown in **b**. The line profiles from which kymographs **1** and **2** were taken are shown as double-sided arrows in the bright-field image. Kymographs **1** and **2** were taken from the stimulated cell and an adjacent cell, respectively. Scale bar (bright-field image), 50 μm. Kymograph **1** shows local contraction in the stimulated cell (top arrow in **1**), indicated by a convergence of the edges in the kymograph plot. Both kymographs **1** and **2** show periodic beating in the stimulated cell and surrounding cell (bottom arrow in **1** and arrow in **2**). **d**–**f**, Normalized fluorescence intensity change of Fluo-4 in cardiomyocytes adjacent to stimulated cardiomyocytes that were treated with MM **1** alone (**d**), MM **1** and U-73 (10 μM) (**e**) and MM **1** in calcium-free PBS (**f**). For each condition, $n = 50$ cells were used. The x-axis label in **f** also applies to **d** and **e**. All the stimulation experiments were performed with a stimulation time of 250 ms at 5.1×10^2 W cm^{-2} in a circular region of 5 μm diameter using a 400 nm laser. In all the plots, the cyan line indicates the time of stimulus presentation.

(Fig. 3b and Supplementary Video 6). This process is dependent on IP_3-mediated signalling (Supplementary Fig. 18). MM-induced calcium release initially leads to localized myocyte contraction at the site of stimulation (Fig. 3c, kymograph 1, top arrow, Supplementary Fig. 19 and Supplementary Video 7), probably due to the calcium-mediated activation of troponin and subsequent actin–myosin cross-bridge formation[36]. Then, SR calcium release induces beating in quiescent cardiomyocytes and accelerated beating in active cardiomyocytes (Fig. 3c, bottom arrow in kymograph 1 and arrow in kymograph 2, and Supplementary Video 8), probably by local membrane depolarization[37].

We tracked the behaviour of cardiomyocytes in contact with cells stimulated with MM and light to determine whether we could use MM to drive biological behaviours coordinated in networks of cells, such as contraction. Colonies of cardiomyocytes adjacent to stimulated cells responded to stimulation by firing action potentials or participating in the generated calcium wave (Fig. 3d, Supplementary Figs. 20–22 and Supplementary Video 9). Activation of adjacent cardiomyocytes in response to stimulation could be prevented by either inhibiting IP_3-mediated calcium release in the stimulated cell (Fig. 3e) or by preventing the influx of calcium from outside the cell during action potential firing (Fig. 3f). Cells stimulated with MM **1** and light exhibited firing rates of 5.1 spikes min^{-1} cell^{-1}, whereas cells stimulated with MM **1** and light in the presence of PLC inhibitor (U-73; 10 μM) exhibited firing rates of 0.8 spikes min^{-1} cell^{-1} ($P < 0.0001$ by a one-tailed Welch's t-test). Meanwhile, cells stimulated in the absence of extracellular calcium did not exhibit any spiking activity. These experiments show that biological behaviours coordinated in the networks of cells, such as contraction, can be controlled by MM-induced calcium wave generation.

MM control behaviour in vivo

Finally, using an in vivo model of muscle contraction, we sought to investigate whether MM-induced ICW can control biological activity at the organism level. For this purpose, we chose *Hydra vulgaris* as a model system. *Hydra* are radially symmetric, millimetre-sized freshwater cnidarians containing tentacles, an oral region and an aboral region connected by a long, tubular body column. In the oral region, *Hydra* have a dome-shaped structure called a 'hypostome' surrounded by a ring of tentacles. At the other extremity, they have a foot called the 'peduncle' (Fig. 4a). *Hydra* were chosen as a model system because of their small size, lack of chitin layer and excitable epitheliomuscular tissue. In addition, *Hydra* exhibit spontaneous and stimulus-controlled contractions, both driven by ICW[38]. In our experiments, we used *Hydra* lines genetically engineered to express the calcium indicator GCaMP7b in their endothelial epitheliomuscular tissue (Methods).

Before the stimulation experiments, *Hydra* were loaded with MM by incubating with solutions containing 24 μM of MM for 24 h (Fig. 4b). Distinct stimulation protocols were employed to cause either local ICW or whole-body contraction (Supplementary Fig. 23). First, the treatment of MM-loaded *Hydra* with pulses of laser light administered to a small region of the body column (protocol **I**) caused ICW emanating from

https://doi.org/10.1038/s41565-023-01436-w

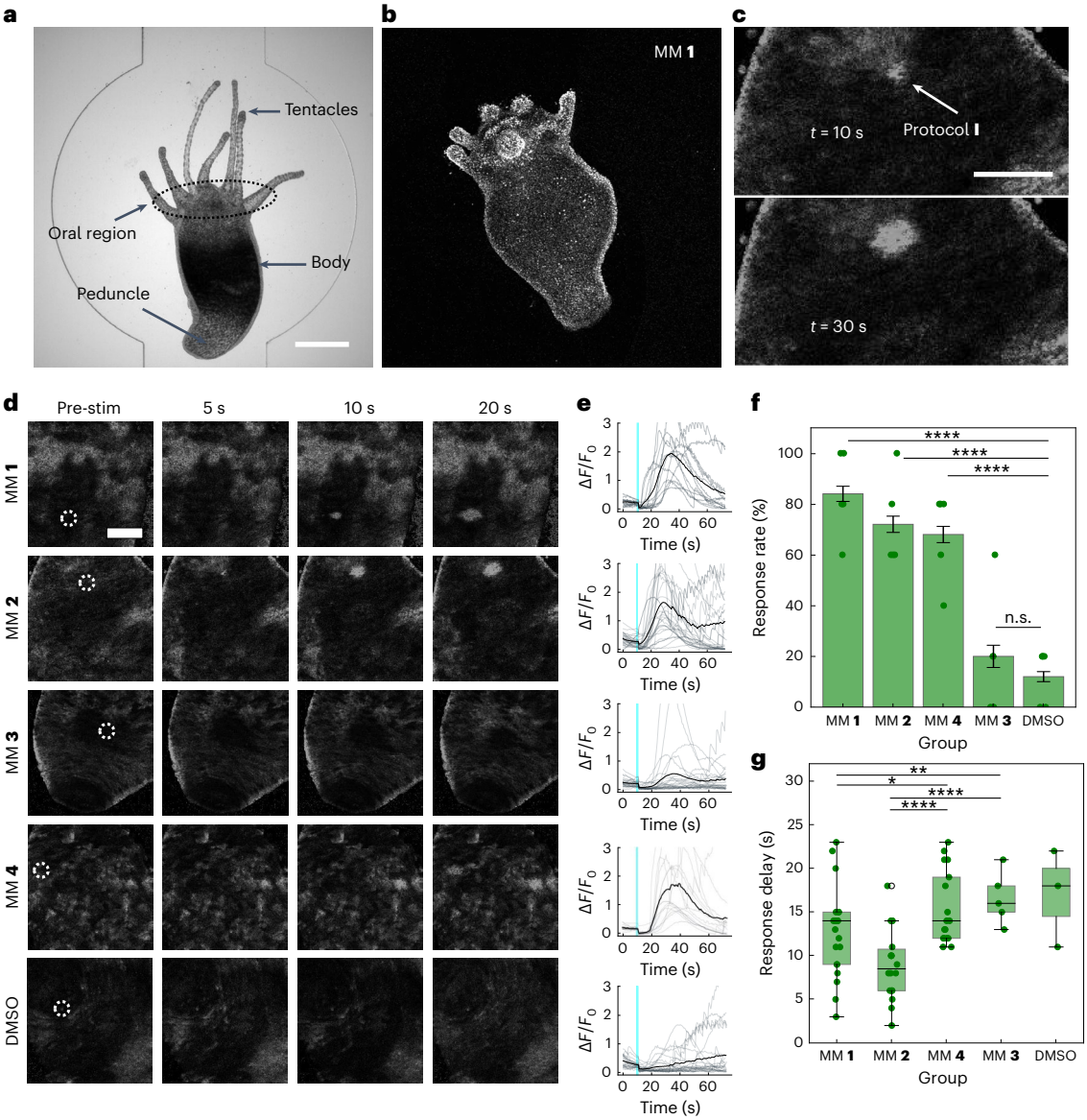

Fig. 4 | MM induce regional calcium waves in vivo. a, Image of *Hydra* loaded into a microfluidic chamber with anatomical regions marked. Scale bar, 100 µm. **b**, MM **1** (24 µM) loaded into *Hydra* for 24 h. **c**, Regional ICW in *Hydra* treated with MM **1** and stimulated with 405 nm light via protocol **I**. The indicated times represent the time after stimulation at which the image was taken. The arrow in the top image indicates the stimulated area. Scale bar, 50 µm. **d**,**e**, Representative images (**d**) and normalized GCaMP7b fluorescence intensity traces (**e**) observed from *Hydra* treated with each MM or DMSO control and stimulated for 1 s using protocol **I**. The bold, black-coloured traces represent the average trace ($n = 25$ across five *Hydra*). The grey traces represent individual experiments. **f**, Bar graph showing the ICW response rate. **g**, Box-and-whisker plot showing the ICW delay time of *Hydra* stimulated using protocol **I** across MM treatment conditions ($n = 25$ experiments across at least five *Hydra* per condition). The ICW responses were defined as $\Delta F/F_0 > 1$. The error bars in **f** represent the standard error of the mean. *P* values for response rate comparisons of MM **1** and DMSO, MM **2** and DMSO and MM **4** and DMSO were $P < 0.0001$. The box-and-whisker plots indicate Q1, median and Q3; whisker lengths extend to 1.5× the interquartile range. *P* values for delay time comparisons of MM **1** and MM **3**, MM **2** and MM **3**, MM **1** and MM **4**, and MM **2** and MM **4** were $P = 0.01871$, $P < 0.0001$, $P = 0.0257$ and $P < 0.0001$, respectively. For all the plots, the cyan lines indicate the time of stimulus with 405 nm light (9.0×10^2 W cm^{-2}), during which no data were collected. The significance tests were conducted using a one-tailed Welch's *t*-test. *P value < 0.05, **P value < 0.01, ***P value < 0.001, ****P value < 0.0001.

the site of stimulation (Fig. 4c and Supplementary Videos 10 and 11). These ICW were robust to anaesthetization of *Hydra* with linalool[39] or 1-heptanol[40] (Supplementary Fig. 24) and exhibited distinct propagation kinetics when different regions of *Hydra* were simultaneously stimulated (Supplementary Video 12).

Second, we attempted to use MM activation to drive whole-body *Hydra* contractions by administering laser stimuli to the oral region (protocol **II**). We targeted the oral region because the mechanical stimulation of this region has been shown to stimulate burst contraction, probably via the sensory neurons that cluster in this region[41–43]. When laser stimuli were delivered to the oral region of *Hydra* treated with fast-rotating MM **1** and **2** (protocol **II**), they exhibited contraction bursts associated with whole-body calcium waves (Supplementary Videos 13 and 14) similar to those observed with macro-mechanical stimulation[44].

Fast-rotating MM were generally more successful in eliciting both regional ICW (protocol **I**) and whole-body contractions (protocol **II**) than slow-rotating MM. Figure 4d,e shows responses from MM-treated *Hydra* when stimulated via protocol **I** to elicit regional ICW. Fast-rotating MM, including MM **1**, MM **2** and even non-unidirectional

https://doi.org/10.1038/s41565-023-01436-w

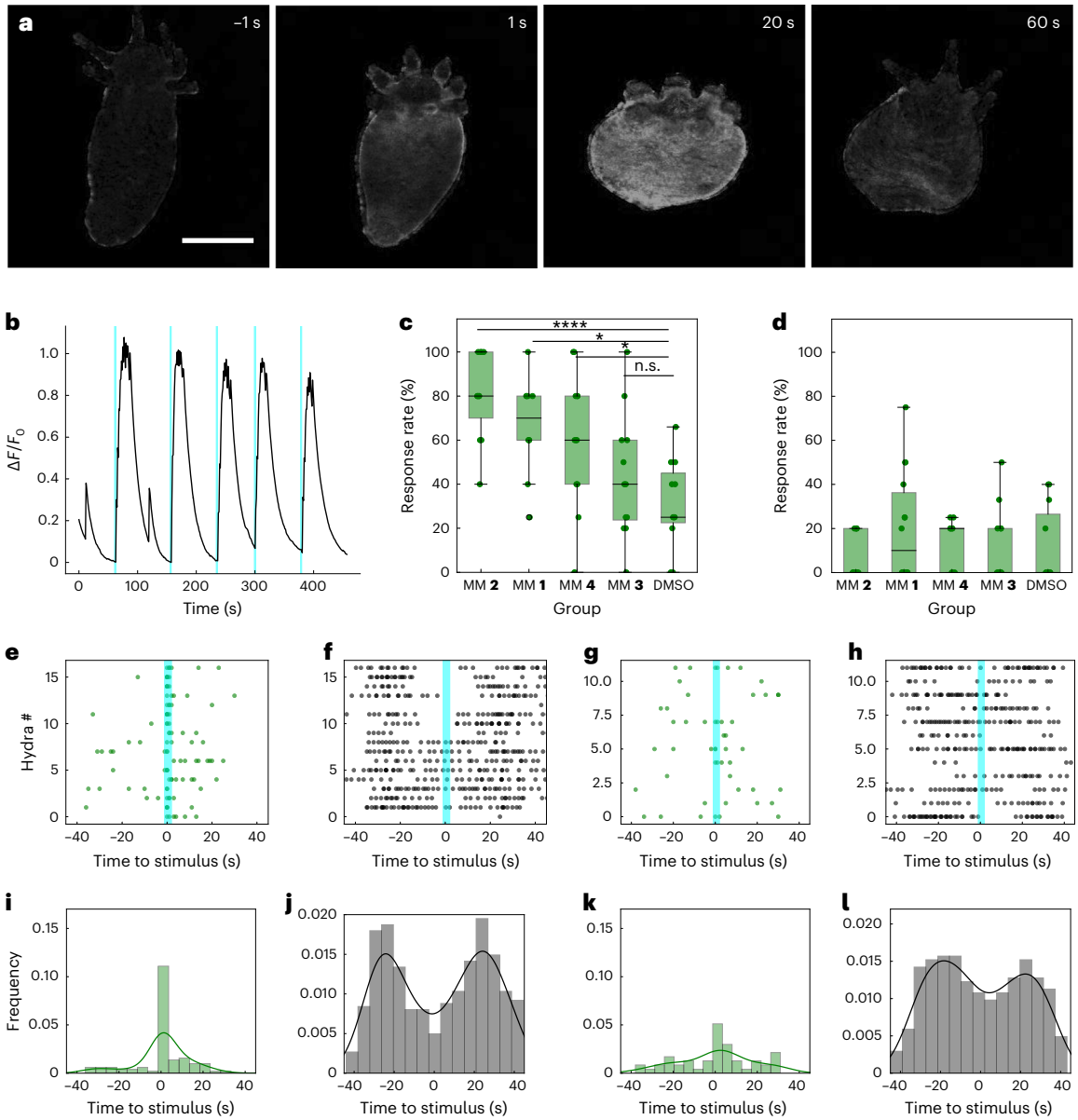

Fig. 5 | MM induce contraction in *H. vulgaris*. **a**, Fluorescence micrographs of a representative *Hydra* contraction. The signal is from GCaMP7b. **b**, Representative GcaMP7b fluorescence trace in a *Hydra* treated with MM **2** and stimulated using protocol **II**. The cyan lines indicate a 2 s stimulus with 405 nm light (9.0×10^2 W cm^{-2}), during which no data were collected. **c**,**d**, Box-and-whisker plots showing contractile response rates across treatment conditions for *Hydra* stimulated for 2 s using protocol **II** (at least 50 experiments across ≥5 *Hydra* per condition) with (**c**) and without (**d**) light. The box-and-whisker plots indicate Q1, median and Q3; whisker lengths extend to 1.5× the interquartile range. The statistical tests were conducted using Fisher's exact test using the proportion of successes and failures for each group. For the comparisons of MM **2**, MM **1** and MM **4** to DMSO, the calculated *P* values were $P < 0.0001$, $P = 0.0199$ and $P = 0.0439$, respectively. **e**–**h**, Scatter plots of contraction onset (**e**) and contraction bursts (**f**) in MM **2** + L-treated *Hydra*, and contraction onset (**g**) and contraction bursts (**h**) in DMSO + L-treated *Hydra*, relative to the time of stimulus presentation. **i**–**l**, Frequency of contraction onsets (**i**) and contraction bursts (**j**) in MM **2** + L-treated *Hydra*, and contraction onsets (**k**) and contraction bursts (**l**) in DMSO + L-treated *Hydra*, relative to the time of stimulus presentation. The contraction onset is shown in green, whereas the contraction bursts are shown in grey or black. Methods provides a detailed description of the response rate calculation.

fast motor MM **4**, consistently elicited robust ICW on the stimulation of the body column (protocol **I**). Weak responses were also observed from *Hydra* treated with slow-rotating MM **3**, although the proportion of these responses that reached a threshold value of $\Delta F/F_0 = 1$ was not statistically significantly different from solvent-only controls (Fig. 4f). *Hydra* also demonstrated marked differences in response kinetics depending on the type of MM employed. Fast, unidirectionally rotating MM elicited appreciably quicker responses (12.76 s for MM **1** and 9.05 s for MM **2**) than slow or non-unidirectionally rotating MM (16.60 s for MM **3** and 15.46 s for MM **4**; Fig. 4g).

Similar trends were observed for whole-body contractile response rates across *Hydra* treated with different MM and light conditions. Figure 5a,b shows a representative whole-body contraction and GCaMP7b fluorescence trace from a typical experiment using MM **2** and stimulation using protocol **II**. In these experiments, the fastest-rotating MM, namely, MM **2**, was the most successful at inducing *Hydra* contraction, demonstrating a response rate of 86% (Fig. 4c,d). This fast-rotating MM elicited the contraction of *Hydra* at a higher rate than light alone ($P < 0.0001$) or slower-rotating MM **3** ($P < 0.0001$). MM **1** also elicited a contraction at a higher rate than light alone ($P = 0.0199 < 0.05$), whereas

the slow-rotating MM **3** ($P = 0.5325 > 0.05$) did not elicit a contraction at a higher rate than light alone. MM **4**, which rotates quickly but non-unidirectionally, elicited *Hydra* contraction with a response rate of 65% and was statistically significantly ($P = 0.0439 < 0.05$) more effective than light alone. Consequentially, rotor speed is a better indicator of the ability of MM to drive *Hydra* contraction than rotor unidirectionality.

Since local ICW can be observed in *Hydra* treated with slow-rotating motors, it is difficult to attribute the entirety of the calcium responses we observe in vivo to the effect of molecular motion. Therefore, secondary mechanisms that are absent in vitro probably contribute to the calcium transients observed in *Hydra*. This hypothesis is supported by experiments with additional slow-rotating and non-rotating molecules, where molecules that absorbed visible light and were inactive in vitro elicited calcium responses in *Hydra* upon photostimulation (Supplementary Figs. 25–28 and the related discussion in Supplementary Information).

However, fast-rotating MM were able to drive stronger and faster signalling cascades in vivo. Additionally, only *Hydra* treated with fast-rotating motors were activated potently enough to stimulate a contractile response (Fig. 5c). This suggests that the molecular-motion-driven effects observed in vitro comprise one of several mechanisms contributing to the observed calcium responses in vivo, and the presence of a fast-rotating MM amplifies the response to a level sufficient to modulate behaviour. Further experiments are needed to elucidate the factors influencing MM propensity for causing ICW in vivo.

Finally, peak identification algorithms were employed to track calcium spikes corresponding to contraction onset and contraction bursts (Fig. 5e–l and Supplementary Figs. 29–33). *Hydra* appeared to exhibit a photic response to light in the absence of MM (Supplementary Fig. 33; $P = 0.0525 > 0.05$) consistent with the photosensitivity of the hypostome and tentacles described previously[45]. However, fast-rotating MM actuation was particularly superior at driving muscle contraction compared with light alone. In *Hydra* treated with MM **2** and light, contraction onset occurs predominantly on the presentation of stimulus, and a high density of contraction bursts appears 5–10 s later (Fig. 5e,f,i,j). In the absence of MM, this relationship weakens dramatically (Fig. 5g,h,k,l). In the absence of light, it disappears completely (Supplementary Fig. 33). These results suggest that the activation of *Hydra* with MM and light was sufficient to control the behavioural phenotypes exhibited by *Hydra* over the timescale of our experiments.

Conclusion

This work demonstrated that the activation of MM by light triggers IP_3-driven calcium waves in a fashion that depends on their rotary properties. In primary rat cardiomyocytes, MM-induced ICW caused localized contraction and action potential firing. In *H. vulgaris*, MM caused regional calcium waves and whole-body contraction. In vitro, only fast, unidirectional MM were able to elicit robust calcium transients. In *Hydra*, slow-rotating MM elicited small transients, but only the fast-rotating MM elicited sufficient calcium release to modulate behaviour. The use of mechanical force delivered by a small molecule to control cell signalling could be a powerful motif for the design of next-generation pharmaceutical targets or bioelectronic devices. However, this method is currently limited by the use of light to drive molecular actuation, and it is unclear how well the effect scales to mammalian in vivo systems. Future work will be pursued to explore how well this strategy scales to mammalian tissues and organisms.

Online content

Any methods, additional references, Nature Portfolio reporting summaries, source data, extended data, supplementary information, acknowledgements, peer review information; details of author contributions and competing interests; and statements of data and code availability are available at https://doi.org/10.1038/s41565-023-01436-w.

References

1. Clapham, D. E. Calcium signaling. *Cell* **131**, 1047–1058 (2007).
2. Tsutsumi, M. et al. Mechanical-stimulation-evoked calcium waves in proliferating and differentiated human keratinocytes. *Cell Tissue Res.* **338**, 99–106 (2009).
3. Screaton, R. A. et al. The CREB coactivator TORC2 functions as a calcium- and cAMP-sensitive coincidence detector. *Cell* **119**, 61–74 (2004).
4. Carrasco, M. A. & Hidalgo, C. Calcium microdomains and gene expression in neurons and skeletal muscle cells. *Cell Calcium* **40**, 575–583 (2006).
5. Glaser, T. et al. ATP and spontaneous calcium oscillations control neural stem cell fate determination in Huntington's disease: a novel approach for cell clock research. *Mol. Psychiatry* **26**, 2633–2650 (2021).
6. Tada, M. & Concha, M. L. Vertebrate gastrulation: calcium waves orchestrate cell movements. *Curr. Biol.* **11**, R470–R472 (2001).
7. McCormack, J. G., Halestrap, A. P. & Denton, R. M. Role of calcium ions in regulation of mammalian intramitochondrial metabolism. *Phys. Rev.* **70**, 391–425 (1990).
8. Leybaert, L. & Sanderson, M. J. Intercellular Ca^{2+} waves: mechanisms and function. *Phys. Rev.* **92**, 1359–1392 (2012).
9. Eng, G. et al. Autonomous beating rate adaptation in human stem cell-derived cardiomyocytes. *Nat. Commun.* **7**, 10312 (2016).
10. Llano, I. et al. Presynaptic calcium stores underlie large-amplitude miniature IPSCs and spontaneous calcium transients. *Nat. Neurosci.* **3**, 1256–1265 (2000).
11. Takano, T. et al. Astrocyte-mediated control of cerebral blood flow. *Nat. Neurosci.* **9**, 260–267 (2006).
12. Drumm, B. T. et al. The effects of mitochondrial inhibitors on Ca^{2+} signalling and electrical conductances required for pacemaking in interstitial cells of Cajal in the mouse small intestine. *Cell Calcium* **72**, 1–17 (2018).
13. Gourine, A. V. et al. Astrocytes control breathing through pH-dependent release of ATP. *Science* **329**, 571–575 (2010).
14. Berridge, M. J. Calcium signaling remodeling and disease. *Biochem. Soc. Trans.* **40**, 297–309 (2012).
15. Stewart, T. A., Yapa, K. T. D. S. & Monteith, G. R. Altered calcium signaling in cancer cells. *Biochim. Biophys. Acta Biomembr.* **1848**, 2502–2511 (2015).
16. Berridge, M. J., Lipp, P. & Bootman, M. D. The versatility and universality of calcium signaling. *Nat. Rev. Mol. Cell Biol.* **1**, 11–21 (2000).
17. Cornell-Bell, A. H. et al. Glutamate induces calcium waves in cultured astrocytes: long-range glial signaling. *Science* **247**, 470–473 (1990).
18. Sanderson, M. J., Charles, A. C. & Dirksen, E. R. Mechanical stimulation and intercellular communication increases intracellular Ca^{2+} in epithelial cells. *Cell Regul.* **1**, 585–596 (1990).
19. Klok, M. et al. MHz unidirectional rotation of molecular rotary motors. *J. Am. Chem. Soc.* **130**, 10484–10485 (2008).
20. García-López, V. et al. Unimolecular submersible nanomachines. synthesis, actuation, and monitoring. *Nano Lett.* **15**, 8229–8239 (2015).
21. García-López, V. et al. Molecular machines open cell membranes. *Nature* **548**, 567–572 (2017).
22. Zheng, Y. et al. Optoregulated force application to cellular receptors using molecular motors. *Nat. Commun.* **12**, 3580 (2021).
23. García-López, V., Liu, D. & Tour, J. M. Light-activated organic molecular motors and their applications. *Chem. Rev.* **120**, 79–124 (2020).
24. Pollard, M. M., Klok, M., Pijper, D. & Feringa, B. L. Rate acceleration of light-driven rotary molecular motors. *Adv. Func. Mater.* **17**, 718–729 (2007).

25. Alaya-Orozco, C. et al. Visible-light-activated molecular nanomachines kill pancreatic cancer cells. *ACS Appl. Mater. Int.* **12**, 410–417 (2020).
26. Kepp, O., Galluzzi, L., Lipinski, M., Yuan, J. & Kroemer, G. Cell death assays for drug discovery. *Nat. Rev. Drug Discov.* **10**, 221–237 (2011).
27. Galbadage, T. et al. Molecular nanomachines disrupt bacterial cell wall, increasing sensitivity of extensively drug-resistant *Klebsiella pneumoniae* to meropenem. *ACS Nano* **13**, 14377–14387 (2019).
28. Santos, A. L. et al. Light-activated molecular machines are fast-acting broad-spectrum antibacterials that target the membrane. *Sci. Adv.* **8**, eabm2055 (2022).
29. Vriens, J., Appendino, G. & Nilius, B. Pharmacology of vanilloid transient receptor potential cation channels. *Mol. Pharmacol.* **75**, 1262–1279 (2009).
30. Hamill, O. P. & McBride, D. W. Jr The pharmacology of mechanogated membrane ion channels. *Pharmacol. Rev.* **48**, 231–252 (1996).
31. Thastrup, O., Cullen, P. J., Drøbak, B. K., Hanley, M. R. & Dawson, A. P. Thapsigargin, a tumor promoter, discharges intracellular Ca^{2+} stores by specific inhibition of the endoplasmic reticulum Ca^{2+}-ATPase. *Proc. Natl Acad. Sci. USA* **87**, 2466–2470 (1990).
32. Bock, G. R. & Ackrill, K. *Calcium Waves, Gradients and Oscillations* (Wiley, 2008).
33. Gafni, J. et al. Xestospongins: potent membrane permeable blockers of the inositol 1,4,5-trisphosphate receptor. *Neuron* **19**, 723–733 (1997).
34. Ribeiro, C. M. P., Reece, J. & Putney, J. W. Role of the cytoskeleton in calcium signaling in NIH 3T3 cells. *J. Biol. Chem.* **272**, 26555–26561 (1997).
35. Xu, J. et al. GPR68 senses flow and is essential for vascular physiology. *Cell* **173**, 762–775.e16 (2018).
36. Feher, J. *Quantitative Human Physiology: An Introduction* 351–361 (Elsevier, 2007).
37. Stuyvers, B. D., Boyden, P. A. & ter Keurs, H. E. D. J. Calcium waves. *Circ. Res.* **86**, 1016–1018 (2000).
38. Wang, H. et al. A complete biomechanical model of Hydra contractile behaviors, from neural drive to muscle to movement. *Proc. Natl Acad. Sci.* **120**, e2210439120 (2023).
39. Goel, T., Wang, R., Martin, S. & Collins, E.-M. S. Linalool acts as a fast and reversible anesthetic in *Hydra*. *PLoS ONE* **14**, e0224221 (2019).
40. Takaku, Y. et al. Innexin gap junctions in nerve cells coordinate spontaneous contractile behavior in *Hydra* polyps. *Sci. Rep.* **4**, 3573 (2014).
41. Kinnamon, J. C. & Westfall, J. A. A three dimensional serial reconstruction of neuronal distributions in the hypostome of a *Hydra*. *J. Morphol.* **168**, 321–329 (1981).
42. Kinnamon, J. C. & Westfall, J. A. Types of neurons and synaptic connections at hypostome-tentacle junctions in *Hydra*. *J. Morphol.* **173**, 119–128 (1982).
43. Dupre, C. & Yuste, R. Non-overlapping neural networks in *Hydra vulgaris*. *Curr. Biol.* **27**, 1085–1097 (2017).
44. Badhiwala, K. N., Primack, A. S., Juliano, C. E. & Robinson, J. T. Multiple neuronal networks coordinate *Hydra* mechanosensory behavior. *eLife* **10**, e64108 (2020).
45. Guertin, S. & Kass-Simon, G. Extraocular spectral photosensitivity in the tentacles of *Hydra vulgaris*. *Comp. Biochem. Physiol. A Mol. Integr. Physiol.* **184**, 163–170 (2015).

Methods

Synthetic chemistry

Details on the synthesis and characterization of MM **2**–**4** are provided in Supplementary Figs. 34–48. Synthesis and characterization information on MM **1** (ref. 25) and control molecules DL-4-762 (ref. 25) and ARV-3-056 (ref. 46), as well as a detailed breakdown of the nuclear magnetic resonance characterization of MM 1 analogues[47], are provided elsewhere. MM were dissolved in dimethyl sulfoxide (DMSO) at a concentration of 8 mM and sonicated for 5 s before use. The MM solutions were stored at −20 °C in aluminium-foil-wrapped containers to avoid degradation. The ultraviolet–visible spectra of MM were taken in spectral-grade water using a Shimadzu UV-3600 Plus spectrophotometer. The fluorescence spectra were taken using a Horiba FluoroMax-4 spectrofluorometer at a 400 nm excitation wavelength. The extinction coefficients were calculated by constructing a Beer's law plot using concentrations between 8 and 32 μM.

Cell culture and preparation of cells for microscopy

HEK293 cells were chosen as the principal model system due to their widespread use in electrophysiological studies. HEK cells, like most excitable or non-excitable cells, are known to exhibit calcium responses[48]. HEK293 cells, HeLa cells and N2A cells were cultured in Dulbecco's modified Eagle's medium (Lonza) supplemented with 10% foetal bovine serum (Gibco) and 1% penicillin–streptomycin (Lonza) at 37 °C in 5% CO_2 atmosphere conditions. The cells were passaged at <90% confluence. To grow cardiomyocytes, a dissolved rat heart (TransnetYX) was triturated, centrifuged and resuspended in a cardiomyocyte growth medium (TransnetYX catalogue #SKU-NBCG) and seeded at a concentration of 60,000 cells cm^{-2}. The growth substrates were pretreated with 1% gelatin solution for 3 h and then washed with phosphate-buffered saline (PBS). Cardiomyocytes were allowed to grow for four days, after which the growth medium was exchanged for cardiomyocyte maintenance medium (TransnetYX catalogue #SKU-NBCM). The experiments were conducted from day 4 to day 6.

Imaging was performed in an imaging extracellular buffer (119 mM NaCl, 5 mM KCl, 10 mM HEPES, 2 mM $CaCl_2$, 1 mM $MgCl_2$ (pH 7.2); 320 mOsm). The cells were prepared for imaging by seeding a 35 mm Ibidi imaging dish with ~50,000 cells in 1 ml of complete growth medium and grown for two days. Before imaging, the cells were incubated with dyes and/or molecules resuspended in the complete growth medium at an appropriate concentration (MM **1** (8 μM), MM **2** (8 μM), MM **3** (24 μM), MM **4** (8 μM) and Fluo-4 (2 μM)). MM and Fluo-4 were incubated with cells for 45 min. For experiments investigating cytoskeleton dynamics, the cells were incubated overnight with CellLight Actin-GFP, BacMam 2.0 (Thermo Fisher catalogue #C10582) a day before the experiment as per the manufacturer's protocol and then incubated with MM **1** for 45 min. For voltage imaging experiments, the cells were incubated with MM **1** and di-8-Anneps for 45 min before the experiment. Unless otherwise specified, all the experiments were performed in triplicate.

In vitro imaging and stimulation

The cells were imaged with a Nikon A1-Rsi confocal system mounted on a wide-field Ti-E fluorescence microscope. Imaging was performed using a ×60 water-immersion objective (numerical aperture, 1.27; working distance, 0.17 mm). Green fluorophores (Fluo-4, MitoTracker Green) were excited with a 488 nm photodiode laser. The red fluorophores (ER-Tracker Red, PI) were excited with a 561 nm photodiode laser. Deep red fluorophores (CellMask plasma membrane stain) were excited with a 630 nm photodiode laser. Laser stimulation for in vitro experiments was performed with a 400 nm photodiode laser (Coherent OBIS^{T} LX SF) operating in the fluorescence-recovery-after-photobleaching experiment mode, delivering up to 6.4×10^2 W cm^{-2} at the sample level. In vitro experiments with HEK293 cells were conducted using a stimulus irradiance of 3.2×10^2 W cm^{-2}, except when indicated otherwise. Cardiomyocyte experiments were conducted using a stimulus irradiance of 5.1×10^2 W cm^{-2}. Power was calibrated using a Thorlabs S130C laser power meter. The stimulation was targeted to a circular area of diameter 5 μm in a 250 ms pulse, during which the laser rastered across the entire region of interest. An additional laser stimulation setup was used to verify the requisite stimulation power and demonstrate excitation in the non-scanning laser mode (Supplementary Fig. 49 and the accompanying discussion). This setup was also used for voltage imaging experiments due to the high temporal resolution it affords. Fluo-4 fluorescence was collected for ~30 s before and 2 min after stimulation (since the recorded time of the first data point is 0 s, stimulation occurs between 28.60 and 28.85 s in the recorded traces). The images were collected using a Galvano scanner operating at 0.94 fps. In some experiments, the images were also collected using a resonant scanner operating at 7.7 fps.

Co-localization analysis

Cells were treated with MitoTracker Green (Thermo Fisher, 400 nM), ER-Tracker Red (Thermo Fisher, 500 nM) and CellMask Deep Red Plasma Membrane Stain (Thermo Fisher, 500 nM). ER-Tracker Red and MitoTracker Green were loaded into cells for 45 min in the complete growth medium. Then, CellMask Deep Red Plasma Membrane Stain was loaded into the cells for 5 min and the cells were subsequently loaded into the microscope chamber. Images for the co-localization analysis were collected in a Nikon A1 confocal microscope using a 60× water-immersion objective. The *Z*-stack images spanning a minimum 20 μm range were collected and processed using the Coloc 2 plugin in Fiji (ImageJ2 version 2.9.0). Co-localized pixel intensity maps were generated using the co-localization threshold function in Fiji.

Pharmacological experiments

In pharmacological blocking experiments, cells were loaded with MM and Fluo-4 as previously described. Typical imaging experiments were then performed on six cells in imaging the extracellular buffer alone as a positive control. Then, the imaging buffer was replaced, and the cells were treated as required for each experiment (see below). After a brief recovery period, six non-previously imaged cells were stimulated and imaged. PBS was used for experiments in the calcium-free buffer. Th (1 μM) and Cyto D (2 μM) were incubated with cells in the incubator in the complete growth medium for 1 h (Th) or 2 h (Cyto D) before imaging. RR (10 μM), Gd^{3+} (50 μM), Ry (100 μM), XeC (20 μM) and U-73 (10 μM) were directly administered into the imaging extracellular buffer after control imaging was finished. The cells were incubated in the medium for ~5 min before imaging. For experiments using reactive oxygen species scavengers, cells were incubated with either melatonin (100 μM), thiourea (50 mM) or L-ascorbic acid (2 mM) for 1 h before the experiments. The traces shown are representative results across at least six cells from individual experiments, whereas bar graphs represent the average results across at least three distinct experiments (Supplementary Table 3).

Measuring cellular uptake

Relative cellular uptake of MM was measured using flow cytometry. HEK293 cells were cultured as described previously and harvested using 0.05% Trypsin-EDTA. The cells were diluted to 2.0×10^5 cells ml^{-1} in Dulbecco's modified Eagle's medium without phenol red (10% foetal bovine serum and 1% penicillin–streptomycin) and incubated with MM **1** (8 μM) for 45 min. The cells were either incubated in a refrigerator (4.0 °C), at room temperature (~23.2 °C) or in an incubator (5% CO_2, 37.0 °C) to give a sense for the temperature dependence of MM loading[49–68]. After incubation, the cells were triturated and loaded into a flow cytometry tube. The cells were loaded into a Sony MA900 multi-application cell sorter. MM fluorescence was detected using a 400 nm laser. At least 10,000 events were recorded.

Hydra preparation

Hydra were grown in a *Hydra* medium containing $CaCl_2{\cdot}2H_2O$ (1.00 mM), $MgCl_2{\cdot}6H_2O$ (0.10 mM), KNO_3 (0.03 mM), $NaHCO_3$ (0.50 mM) and $MgSO_4$ (0.08 mM) in deionized water at 18 °C in a light-cycled (12 h light, 12 h dark) incubator. *Hydra* were fed with an excess of freshly brined *Artemia nauplii* (Brine Shrimp Direct, Ogden, UT, #BSEP 8Z) three times a week. All the experiments were performed at room temperature after starving the animals for two days. The transgenic line expressing the calcium indicator GCaMP7b under the Ef1α promoter in endodermal epitheliomuscular tissue was generated by embryonic microinjection in collaboration with the Robinson lab (Rice University) and Juliano lab (University of California, Davis)[42].

Hydra imaging and stimulation

Hydra were incubated with the selected MM for 24 h before imaging. The stimuli were applied using a region-of-interest-driven fluorescence-recovery-after-photobleaching mode in a Nikon A1 confocal microscope. All the *Hydra* were able to recover after the stimulation experiments, indicating that both MM administration and subsequent stimulation treatments were not toxic to *Hydra*.

Distinct stimulation protocols were employed to elicit either regional ICW or whole-body contraction. In protocol **I**, stimulation was delivered using a 405 nm laser diode at 9.0×10^2 W cm^{-2} in 1 s pulses delivered to a 10 µm region of the *Hydra* body column. Protocol **I** resulted in regional ICW. In protocol **II**, stimulation was delivered using a 405 nm laser diode at 9.0×10^2 W cm^{-2} in a 2 s pulse delivered to the oral region of the *Hydra* (typical area, ~1,000–2,000 µm^2). Protocol **II** resulted in whole-body calcium waves and contraction. Note that despite the longer stimulation time used in protocol **II**, the *Hydra* still experiences less pixel dwell time and less incident light per unit area compared with in vitro experiments and protocol **I** due to the size of the stimulation region (~50–100 times larger depending on the size of the animal). GCaMP7b fluorescence was recorded using a 456 nm laser diode for fluorophore excitation. In experiments using protocol **I**, the stimuli were presented at 10 s. In experiments using protocol **II**, the stimuli were presented at irregular intervals at least 60 s apart to prevent interference from periodic spontaneous contractions of *Hydra*.

Data analysis

Data were analysed using custom-written Python scripts (version 3.8.3). Fluorescence traces of the calcium indicator Fluo-4 from the cells were imported and processed using the Pandas library. Here F_0 was calculated as the average fluorescence intensity in the first ten frames (~10 s) of the acquisition and used to calculate $\Delta F/F_0$ over the entire length of the acquisition. Since data were not collected during stimulation, a 'dead time' equivalent to the time of stimulation was manually added to each recording. The spiking behaviour of cardiomyocytes was calculated using the SciPy peak finder function.

Fluorescence traces of calcium indicator GCaMP7b in *H. vulgaris* were processed similar to the in vitro data and baseline corrected to set the minimum measured $\Delta F/F_0$ value as '0' due to the spontaneous, periodic activity of the *Hydra*. For experiments analysing regional ICW (stimulating using protocol **I**), responses reaching $\Delta F/F_0 > 1$ in the stimulated area were considered a 'success' in the calculation of the ICW response rate. The 'delay time' was the time at which $\Delta F/F_0$ reached 1. The peaks corresponding to whole-body contraction were not included in the analysis of the ICW amplitude. The ICW response rate was calculated across $n = 25$ experiments for each condition across at least five *Hydra*.

In experiments analysing whole-body contraction (stimulating using protocol **II**), the induction of a contractile 'response' comprising a change in body GCaMP7b fluorescence of $\Delta F/F_0 > 1.5\times$ within 3 s of stimulus presentation was counted as a 'success' in the calculation of the contractile response rate. To identify contraction onset, a limit-of-detection peak finding algorithm was used with a threshold value of 1.5. To identify individual calcium spikes in a contraction burst, the SciPy peak finder function was employed. The induction of a contractile 'response' comprising a change in body GCaMP7b fluorescence of $\Delta F/F_0 > 1.5\times$ within 3 s of stimulus presentation was considered a 'success' when calculating the response rates. The response rates were calculated over at least 50 presentations of stimuli. The stimuli presented at a time when the *Hydra* were already contracting ($\Delta F/F_0 > 0.3$) were discarded. *Hydra* that exhibited mouth-opening behaviour during the experiment were discarded. The effects of spontaneous and photic responses were accounted for by comparison with DMSO and DMSO plus light controls. Supplementary Table 4 provides more information on *Hydra* data processing.

Statistical analysis

One-tailed Welch's *t*-tests were performed to assess differences in cellular responses after pharmacological manipulations, or when treated with MM of different rotation speeds. Fisher's exact tests were used to assess differences in contractile response rates between *H. vulgaris* treated with MM of variable rotation speed and light. $^*P$ value < 0.05, $^{**}P$ value < 0.01, $^{***}P$ value < 0.001, $^{****}P$ value < 0.0001.

Reporting summary

Further information on research design is available in the Nature Portfolio Reporting Summary linked to this article.

Data availability

All data supporting the findings of this study are available within the article and its supplementary information. Source data are provided with this paper. Additional raw data and analysis code are available via GitHub at https://github.com/jlb48249/MM-ICW.

Code availability

Data analysis scripts are available via GitHub at https://github.com/jlb48249/MM-ICW.

References

46. van Venrooy, A. et al. Probing the rotary cycle of amine-substituted molecular motors. *J. Org. Chem.* **88**, 762–770 (2023).
47. Garcia-Lopez, V. et al. Synthesis of light-driven motorized nanocars for linear trajectories and their detailed NMR structural determination. *Tetrahedron* **73**, 4864–4873 (2017).
48. Sinnecker, D. & Schaefer, M. Real-time analysis of phospholipase C activity during different patterns of receptor-induced Ca^{2+} responses in HEK293 cells. *Cell Calcium* **35**, 29–38 (2004).
49. Lancon, A. et al. Human hepatic cell uptake of resveratrol: involvement of both passive diffusion and carrier-mediated process. *Biochem. Biophys. Res. Commun.* **4**, 1132–1137 (2004).
50. Roke, D. et al. Light-gated rotation in a molecular motor functionalized with a dithienylethene switch. *Angew. Chem. Int. Ed.* **57**, 10515–10519 (2018).
51. Saywell, A. et al. Light-induced translation of motorized molecules on a surface. *ACS Nano* **10**, 10945–10952 (2016).
52. Frisch, M. J. et al. Gaussian 16 Rev. A.03 (Wallingford, 2016).
53. Dennington, R., Keith, T. A and Millam, J. M. GaussView version 6 (Semichem, 2019).
54. Tao, J., Perdew, J. P., Staroverov, V. N. & Scuseria, G. E. Climbing the density functional theory ladder: nonempirical meta-generalized gradient approximation designed for molecules and solids. *Phys. Rev. Lett.* **91**, 146401 (2003).
55. Weigend, F. & Ahlrichs, R. Balanced basis sets of split valence, triple zeta valence and quadruple zeta valence quality for H to Rn: design and assessment of accuracy. *Phys. Chem. Chem. Phys.* **7**, 3297–3305 (2005).

56. Grimme, S., Ehrlich, S. & Georigk, L. Effect of the damping function in dispersion corrected density functional theory. *J. Comp. Chem.* **32**, 1456–1465 (2011).
57. Dunlap, B. I. Robust and variational fitting: removing the four-center integrals from center stage in quantum chemistry. *J. Mol. Struct. THEOCHEM* **529**, 37–40 (2000).
58. Grimme, S., Antony, J., Ehrlich, S. & Krieg, H. A consistent and accurate ab initio parametrization of density functional dispersion correction (DFT-D) for the 94 elements H-Pu. *J. Chem. Phys.* **132**, 154104 (2010).
59. Stratmann, R. E., Scuseria, G. E. & Frisch, M. J. Achieving linear scaling in exchange-correlation density functional quadratures. *Chem. Phys. Lett.* **257**, 213–223 (1996).
60. Zhao, X., Fan, B., Hassan, S., Veeraraghavan, A. & Robinson, J. T. Near field optical sensing of single cell activity with integrated micro-ring resonators. In *Biophotonics Congress 2021* paper BTu3B.4 (Optical Society of America, 2021).
61. Gunasekera, R. S. et al. Molecular nanomachines can destroy tissue or kill multicellular eukaryotes. *ACS Appl. Mater. Int.* **12**, 13657–13670 (2020).
62. Hajnoczky, G., Davies, E. & Madesh, M. Calcium signaling and apoptosis. *Biochem. Biophys. Ref. Commun.* **304**, 445–454 (2003).
63. Cnossen, A., Kistemaker, J. C. M., Kojima, T. & Feringa, B. L. Structural dynamics of overcrowded alkene-based molecular motors during thermal isomerization. *J. Org. Chem.* **79**, 927–935 (2014).
64. Nagaraja, D. et al. Solvent effect on the relative quantum yield and fluorescence quenching of a newly synthesized coumarin derivative. *Luminescence* **30**, 495–502 (2014).
65. Tzouanas, C. N. et al. *Hydra* show stable responses to thermal stimulation despite large changes in the number of neurons. *iScience* **24**, 102490 (2021).
66. Grunder, S. & Assmann, M. Peptide-gated ion channels and the simple nervous system of *Hydra*. *J. Exp. Biol.* **218**, 551–561 (2015).
67. Grigoryan, B. et al. Development, characterization, and applications of multi-material stereolithography bioprinting. *Sci. Rep.* **11**, 3171 (2021).
68. Mizuno, K., Kurokawa, K. & Ohkuma, S. Regulation of type 1 IP_3 receptor expression by dopamine D2-like receptors via AP-1 and NFATc4 activation. *Neuropharmacology* **71**, 264–272 (2013).

Acknowledgements

This project received funding from the Discovery Institute, the Robert A. Welch Foundation (C-2017-20190330), the National Science Foundation Graduate Research Fellowship Program (J.L.B.), the DEVCOM Army Research Laboratory under Cooperative Agreement W911NF-18-2-0234 (A.R.v.V.) and the European Union's Horizon 2020 research and innovation programme under the Marie Skłodowska-Curie grant agreement no. 843116 (A.L.S.). The views and conclusions contained in this document are those of the authors and should not be interpreted as representing the official policies, either expressed or implied, of the Army Research Laboratory or the US government. The US government is authorized to reproduce and distribute reprints for government purposes notwithstanding any copyright notation herein. The funders had no role in the study design, data collection and analysis, decision to publish, or preparation of the manuscript. This work was conducted in part using resources from the Light Microscopy Facility and the Shared Equipment Authority at Rice University. We acknowledge Z. C. Sanchez (Vanderbilt University) for useful help and advice regarding the growth and activity of cardiomyocytes.

Author contributions

Conceptualization: J.L.B., A.R.v.V. and J.M.T. Methodology: J.L.B., G.D., S.K., X.Z. and A.L.S. Organic synthesis: A.R.v.V., G.L., B.L., D.L. and J.M.T. Formal analysis: J.L.B. Investigation: J.L.B., S.K., G.C., D.A. and J.Z. Resources: J.T.R. and J.M.T. Writing (original draft): J.L.B. Writing (reviewing and editing): J.L.B., G.D., S.K., A.L.S., J.T.R. and J.M.T. Software: J.L.B. and J.T.L. Visualization: J.L.B. Supervision: G.D., J.T.R. and J.M.T. Funding acquisition: J.M.T. Project oversight: J.M.T.

Competing interests

Rice University owns the intellectual property on the use of electromagnetic (light) activation of MM for the stimulation of ICW. Conflicts of interest are managed through regular disclosure to the Rice University Office of Sponsored Projects and Research Compliance. The authors declare no other competing interests.

Additional information

Supplementary information The online version contains supplementary material available at https://doi.org/10.1038/s41565-023-01436-w.

Correspondence and requests for materials should be addressed to Jacob T. Robinson or James M. Tour.

Peer review information *Nature Nanotechnology* thanks Carson Bruns, Danijela Gregurec and Gabriela Romero Uribe for their contribution to the peer review of this work.

nature portfolio

Corresponding author(s): tour@rice.edu

Last updated by author(s): 2023/4/13

Reporting Summary

Nature Portfolio wishes to improve the reproducibility of the work that we publish. This form provides structure for consistency and transparency in reporting. For further information on Nature Portfolio policies, see our Editorial Policies and the Editorial Policy Checklist.

Statistics

For all statistical analyses, confirm that the following items are present in the figure legend, table legend, main text, or Methods section.

n/a	Confirmed	
☐	☒	The exact sample size (*n*) for each experimental group/condition, given as a discrete number and unit of measurement
☐	☒	A statement on whether measurements were taken from distinct samples or whether the same sample was measured repeatedly
☐	☒	The statistical test(s) used AND whether they are one- or two-sided *Only common tests should be described solely by name; describe more complex techniques in the Methods section.*
☐	☒	A description of all covariates tested
☐	☒	A description of any assumptions or corrections, such as tests of normality and adjustment for multiple comparisons
☐	☒	A full description of the statistical parameters including central tendency (e.g. means) or other basic estimates (e.g. regression coefficient) AND variation (e.g. standard deviation) or associated estimates of uncertainty (e.g. confidence intervals)
☐	☒	For null hypothesis testing, the test statistic (e.g. *F*, *t*, *r*) with confidence intervals, effect sizes, degrees of freedom and *P* value noted *Give P values as exact values whenever suitable.*
☒	☐	For Bayesian analysis, information on the choice of priors and Markov chain Monte Carlo settings
☒	☐	For hierarchical and complex designs, identification of the appropriate level for tests and full reporting of outcomes
☒	☐	Estimates of effect sizes (e.g. Cohen's *d*, Pearson's *r*), indicating how they were calculated

Our web collection on statistics for biologists contains articles on many of the points above.

Software and code

Policy information about availability of computer code

Data collection	Nikon software was used to run the microscope collecting data.
Data analysis	Fiji was used to process image data. Custom scripts were used to process the data, especially for peak identification. These scripts are available on Github.

For manuscripts utilizing custom algorithms or software that are central to the research but not yet described in published literature, software must be made available to editors and reviewers. We strongly encourage code deposition in a community repository (e.g. GitHub). See the Nature Portfolio guidelines for submitting code & software for further information.

Data

Policy information about availability of data

All manuscripts must include a data availability statement. This statement should provide the following information, where applicable:

- Accession codes, unique identifiers, or web links for publicly available datasets
- A description of any restrictions on data availability
- For clinical datasets or third party data, please ensure that the statement adheres to our policy

All data supporting the findings of this study are available within the article and its supplementary information files. Source data are provided with this paper. Additional raw data and analysis code are available on GitHub at https://github.com/jlb48249/MM-ICW.

Research involving human participants, their data, or biological material

Policy information about studies with human participants or human data. See also policy information about sex, gender (identity/presentation), and sexual orientation and race, ethnicity and racism.

Reporting on sex and gender	No human participants were employed in this study.
Reporting on race, ethnicity, or other socially relevant groupings	No human participants were employed in this study.
Population characteristics	No human participants were employed in this study.
Recruitment	No human participants were employed in this study.
Ethics oversight	No human participants were employed in this study.

Note that full information on the approval of the study protocol must also be provided in the manuscript.

Field-specific reporting

Please select the one below that is the best fit for your research. If you are not sure, read the appropriate sections before making your selection.

☒ Life sciences ☐ Behavioural & social sciences ☐ Ecological, evolutionary & environmental sciences

For a reference copy of the document with all sections, see nature.com/documents/nr-reporting-summary-flat.pdf

Life sciences study design

All studies must disclose on these points even when the disclosure is negative.

Sample size	For Hydra and cardiac myocytes, sample sizes were determined based on relevant literature.
Data exclusions	In Hydra contraction experiments (Fig. 5), stimuli presented during a Hydra contraction were excluded. These exclusions are incorporated into the code and data presented on GitHub, and criteria for exclusion are presented in the manuscript.
Replication	Many of the pharmacology experiments were affirmed by multiple coauthors during triplicate experiments. All attempts at replication were successful.
Randomization	Allocation of cells and Hydra to experimental groups was random.
Blinding	Investigators were not blinded to sample status during data collection.

Reporting for specific materials, systems and methods

We require information from authors about some types of materials, experimental systems and methods used in many studies. Here, indicate whether each material, system or method listed is relevant to your study. If you are not sure if a list item applies to your research, read the appropriate section before selecting a response.

Materials & experimental systems

n/a	Involved in the study
☒	☐ Antibodies
☒	☐ Eukaryotic cell lines
☒	☐ Palaeontology and archaeology
☐	☒ Animals and other organisms
☒	☐ Clinical data
☒	☐ Dual use research of concern
☒	☐ Plants

Methods

n/a	Involved in the study
☒	☐ ChIP-seq
☒	☐ Flow cytometry
☒	☐ MRI-based neuroimaging

Animals and other research organisms

Policy information about studies involving animals; ARRIVE guidelines recommended for reporting animal research, and Sex and Gender in Research

Laboratory animals	Hydra vulgaris (mature adult polyps- Hydra are technically immortal so age is not typically kept).
Wild animals	The study did not involve wild animals.
Reporting on sex	Sex was not considered in the design because Hydra do not exhibit distinct sexes.
Field-collected samples	This study did not involve samples collected from the field.
Ethics oversight	This study did not require regulatory approval since it used invertebrate model species.

Note that full information on the approval of the study protocol must also be provided in the manuscript.